

Growth and structural properties of CuAg and CoPt bimetallic nanoparticles

Cyril Langlois,^{*a} Damien Alloyeau,^{ab} Yann Le Bouar,^b
Annick Loiseau,^b Tetsuo Oikawa,^c Christine Mottet^d and
Christian Ricolleau^a

Received 18th April 2007, Accepted 26th June 2007

First published as an Advance Article on the web 21st September 2007

DOI: 10.1039/b705912b

Core/shell CuAg and alloyed CoPt have been synthesized using two vapor phase deposition techniques. For CuAg prepared by Thermal Evaporation (TE), the size and the morphology of the Cu cores are the key parameters to promote the formation of the core/shell arrangement. For CoPt synthesized by Pulsed Laser Deposition (PLD), the growth kinetics of nanoparticles, depending on the deposition rate, the substrate nature and the temperature, controls the nanoparticle morphology. The competition between the growth and the ordering kinetics governs the nanoparticle structure. By reducing the growth kinetics, as-grown L1₀ ordered nanoparticles are obtained according to the bulk phase diagram.

A. Introduction

Multi-component nanostructures have recently attracted much attention, from both the experimental and theoretical points of view, since it is possible to enhance or to obtain new physical and chemical properties that cannot be obtained in single component nanoparticles. When metals are combined in core/shell configurations or alloyed structures, one can observe dramatic changes in chemical,^{1–4} magnetic^{5,6} and optical properties^{7–9} compared to those of the individual component. This is in addition to the size which directly influences the physico-chemical properties when the characteristic length of a physical property becomes similar to or larger than the particle size.

For both fundamental and technological purposes, new developments are strongly dependent on the ability to have accurate control on the growth of nanoparticles. It is essential to control chemical composition, crystallography, mean size, size distribution and morphology to tailor the physical and chemical properties of the nanoparticles. Up to now, bimetallic core/shell or alloyed nanostructures have been synthesized by several chemical and physical methods: colloids chemistry,^{10,11} ion implantation,¹² as well as vapour phase deposition techniques like sputtering^{13,14}

^a Laboratory Materials and Quantum Phenomena, University Paris 7, 2 Place Jussieu, Paris, France. E-mail: Cyril.Langlois@paris7.jussieu.fr; Fax: +33 1 40 79 47 30; Tel: +33 1 40 79 58 10

^b Laboratory for Microstructural Investigations—ONERA-CNRS, B.P., 92322 Châtillon France. E-mail: Damien.Alloyeau@onera.fr; Fax: +33 1 56 73 41 55; Tel: +33 6 62 64 12 22

^c JEOL Ltd, 1-2 Musashino 3-Chome, Akishima, Tokyo 196-8558, Japan. E-mail: oikawa@jeol.co.jp; Fax: +81 42 546 8063; Tel: +81 42 542 2152

^d CRMCN-CNRS, Campus de Luminy, Case 913 13288, Marseille Cedex 9, France. E-mail: mottet@crmcn.univ-mrs.fr; Fax: +33 4 91 41 89 16; Tel: +33 6 60 30 28 09

and electron-beam evaporation.^{15,16} Among the vapour phase deposition techniques, multiple targets sequential pulsed laser deposition (PLD) has appeared to be one of the most flexible and promising growth techniques because of its capability to control the synthesis by varying parameters such as the laser energy, the pulse repetition rate and fluence (*i.e.* energy density), the target to substrate distance, *etc.* This technique has been widely and successfully used in the preparation of monometallic and semiconductor nanoparticles as well as thin oxide films with controlled composition due to its ability to reproduce very well the stoichiometry of the ablated target.¹⁷

In this paper, we investigate the growth and the structural properties of core/shell CuAg and alloyed CoPt nanoparticles prepared by thermal evaporation (TE) and pulsed laser deposition techniques, respectively. For the CuAg system, we report on the size effects governing the core/shell arrangement, through the study of morphological transitions of the Cu cores depending on their sizes. Concerning the CoPt nanoparticles, we present the influence of the substrate and the laser frequency of the PLD experiment on the growth and the structure of the nanoparticles. We will show how it is possible, by controlling the growth kinetics of nanoparticles, to control the structure and the morphology of the nanoparticles.

B. Experimental

CuAg and CoPt nanoparticles have been prepared on amorphous substrates using the same ultra-high vacuum (UHV) chamber either by classical thermal evaporation or pulsed laser deposition. During the evaporation, the residual pressure in the chamber is close to 10^{-8} mbar. The growth of the nanoparticles has been performed on two different substrates: a 10 nm thick amorphous carbon film (a-carbon) of a commercial 3 mm Cu grid or a 2 nm layer of amorphous alumina (a- Al_2O_3), deposited using PLD on top of the amorphous carbon. The deposition rate of each element is controlled by an *in situ* quartz crystal monitor, which indicates the nominal thickness of deposited materials on the quartz surface, in a continuous thin film approximation. As the metallic species do not wet the two amorphous substrates used here, nanoparticles are formed instead of continuous thin films and the nominal thickness of a sample obviously does not correspond to the particle thickness. During the deposition, the substrate is held at a fixed temperature T_s , between 25 °C and 750 °C. The heating system is a tungsten filament heated by the Joule effect, positioned just behind the TEM grid. The heat transfer occurs through radiation from the filament to the substrate and conduction from the substrate to the particles. At the end of the synthesis, samples were covered by a 3 nm thick a- Al_2O_3 layer deposited by PLD, in order to protect the nanoparticles from air oxidation. Nevertheless, the high vacuum conditions of the deposition chamber offer the possibility to anneal *in situ* the synthesized particles before the deposition of the protective amorphous alumina layer.

1. Thermal evaporation

The sources were Knudsen type cells containing high purity Cu and Ag pellets heated at 1040 °C and 970 °C, respectively. Copper was first evaporated to form pure Cu nanoparticles at the surface of the a-carbon substrate. In a second step, Ag was evaporated. Typically, deposition rates for Cu and Ag were around 0.25 nm per min. During the deposition of Cu and Ag, the substrate is heated at a temperature of 400 °C. This allows the diffusion of the two species on the surface of the substrate. The nanoparticles are annealed during half an hour at the same temperature.

2. Pulsed laser deposition

A typical target–substrate holder configuration is used to deposit separately the a- Al_2O_3 , Co and Pt by PLD, using a KrF excimer laser at 248 nm. The pulse

duration is 25 ns and the repetition rate is in the range of 1 to 15 Hz. The laser irradiation produces the plasma of the different species and vaporised atoms condense on the substrate placed at 5 cm from the target. The growth of the CoPt nanoparticles has been performed on amorphous carbon and amorphous alumina. CoPt nanoparticles are obtained by alternated irradiation of two pure metal targets allowing a composition controlled synthesis.^{18,19} To ensure a good homogeneity of the particle composition, the nominal thickness of deposited materials at each successive step (corresponding to one series of laser pulses on Co and Pt targets) is set to 0.1 nm. The number of pulses on Co and Pt targets at each step was fixed in order to obtain a composition close to Co₅₀Pt₅₀. The laser energy can be chosen in the range of 150 to 250 mJ depending on the ablation threshold of the selected target. The deposition rate depends on the target nature, the energy and the frequency of the laser. We used energies of 190 mJ and 250 mJ for the cobalt and the platinum targets, respectively. These selected energies avoid the formation of micrometric droplets and minimizes the deposition rate which is, as we will show, a key parameter to control particle morphology. With this configuration, deposition rates for Co and Pt were, respectively 0.30 and 0.04 nm min⁻¹.

3. Characterisation tools

Structural characterisations of the nanoparticles were performed using several TEM techniques: conventional Bright Field imaging (BF), High Resolution imaging (HRTEM), Energy Filtered imaging (EFTEM) and electron tomography. The microscopes used for these studies were a JEOL JEM-2100F and a ZEISS LIBRA 200 FE field-emission TEM operating at 200 keV.

C. CuAg Core/shell nanoparticles

Success in obtaining bimetallic core/shell nanoparticles by a physical route mainly depends on: (1) the miscibility of the two metals, (2) the surface energies of those metals and (3) the interfacial energies between a substrate and the two metals. The CuAg system was chosen as a model because of silver and copper being immiscible elements (0.1% solid solution at 298 K). A lower surface energy for Ag (1210 mJ m⁻² compared to 2130 mJ m⁻² for Cu)²⁰ favours the silver surface segregation. CuAg core/shell nanoparticles are then expected to be formed on the amorphous carbon substrate, with Cu core and Ag shell. To improve the efficiency of the core/shell formation, a sequential procedure has been used during the thermal evaporation, with deposition of Cu firstly, and Ag in a second step.

1. 6@3 system

Nominal thicknesses of 6 nm and 3 nm for Cu and Ag, respectively were deposited and we obtained nanoparticles sizes around 25 nm (Fig. 1a). In order to study the growth of core/shell nanoparticles on the substrate, the samples (denoted 6@3 in the following) were fully characterised by transmission electron microscopy. The EFTEM technique was particularly efficient to identify the Ag shells and the Cu cores. For each element, a chemical map was obtained on which the black and white contrast corresponds to the localisation of the selected element (Fig. 1b and c). Gathering together the Cu and Ag chemical maps results in a color coded image as the one presented on Fig. 1d for the 6@3 system. Such chemical information cannot be obtained directly from the classical BF image (Fig. 1a) since it shows no contrast between the two elements.

Many different configurations regarding the silver localisation are noticed. Silver can form continuous shells around the Cu cores, as expected from the thermodynamical considerations discussed previously, but as well silver can grow either independently from the Cu cores, forming pure silver nanoparticles, or onto the Cu

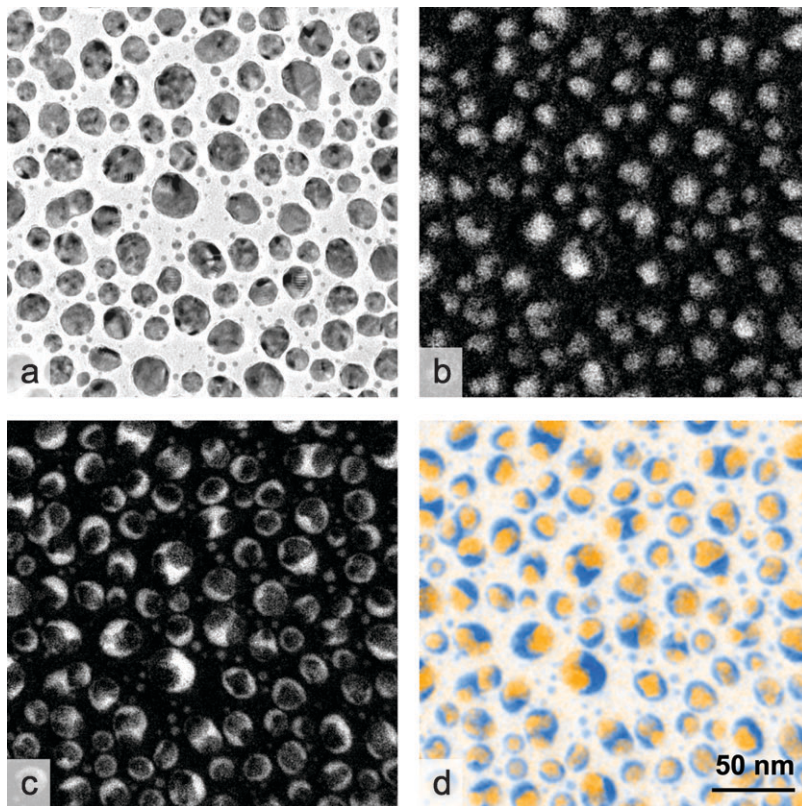


Fig. 1 (a) BF conventional TEM image of an area on the 6@3 sample, (b) Cu chemical map of the same area obtained by EFTEM, (c) Ag chemical map and (d) Colour-coded chemical map with Ag (blue) and Cu (yellow). Note the presence of pure Ag nanoparticles that have nucleated separately on the substrate.

cores, but only on one side of the Cu nanoparticles. The EFTEM images can hardly bring proof of a covering of the Cu cores by Ag because of the projection along the z axis perpendicular to the substrate to form the images. The complete capping of the Cu core by the Ag shell is evidenced by a well-known optical effect called ‘Moiré patterns’ that can be seen on HRTEM or even conventional TEM images (Fig. 2a). Large dark stripes superimposed on to the lattice fringes of the crystal arise when two crystals are overlapped. These patterns appear when interferences occur between two slightly different spatial frequencies (in orientation and/or spacing) in the reciprocal space. Here, the Moiré patterns originate from the epitaxial relationship between the core and the shell.

The crystallographic orientation is the same for the core and the shell, and this was noticed for all the observed nanoparticles. This can be seen on the power spectrum on Fig. 2b, on which Ag and Cu crystals are oriented along the same $[110]$ zone axis of the Face Centred Cubic (FCC) structure, with the same radial orientation of the 200 reflections of the two crystals. The mirror corresponding to the twin plane is reported on the power spectrum. This is a striking example of the shell following exactly the underlying defect of the core.

On Fig. 3, showing a CuAg nanoparticle for which silver did not form a perfect shell around the core, the same epitaxial relationship is reported on the $[100]$ zone axis given in the inset of Fig. 3b. Because of the difference in lattice parameters between the two materials, interfacial edge dislocations would be expected. Since the interface between the two crystals lies on a (220) plane, we carried out a Bragg

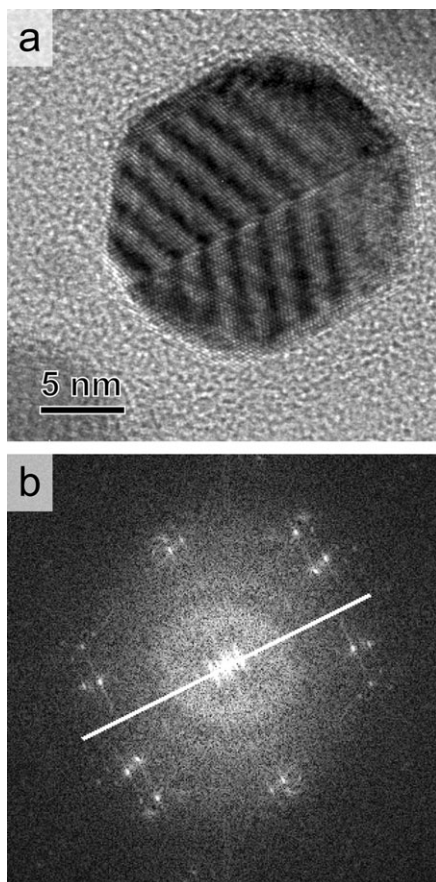


Fig. 2 (a) High resolution image of a CuAg nanoparticle of the 6@3 system, oriented along the [110] zone axis. Moiré patterns show that the silver shell caps completely the Cu core. (b) Power spectrum of the previous image that emphasize the epitaxial relationship between the core and the shell. The power spectrum shows a symmetry mirror (highlighted by a white line on the figure) coming from the twin boundary.

filtering of the image using the 220 type reflections of Cu and Ag. This allows to evidence the localisation of the excess (220) Cu planes composing the misfit dislocations. On Bragg-filtered images (Fig. 3b), the interfacial dislocations spacing is 1.1 nm, that is, around 8 $(220)_{\text{Ag}}$ interplane distances. When estimating the number of (220) planes between interfacial dislocations for an Ag film grown on a Cu film along the [220] direction from the simple formula:²¹

$$n = d_{(220)\text{Ag}} / (d_{(220)\text{Cu}} - d_{(220)\text{Ag}})$$

one would find $n = 8$. The rule of thumb used here is still valid at the nanoscale because we found the same dislocations periodicity on the image. This is a surprising situation since dislocations are usually attracted to free surfaces in order to decrease the elastic field around their core. Here, the epitaxial stress is important enough (a_{Ag} is 11% larger than a_{Cu}) to maintain six perfect dislocations inside approximately a $5 \times 5 \times 5 \text{ nm}^3$ volume. The presence of interfacial dislocations reveals also that Ag and Cu have recovered their own lattice parameter. This has been verified by checking the lattice parameters on both sides of the nanoparticles. This is coherent with another simple model used for heteroepitaxial films, giving the critical thickness over which the interface is no more coherent and misfit dislocations appear.²² This

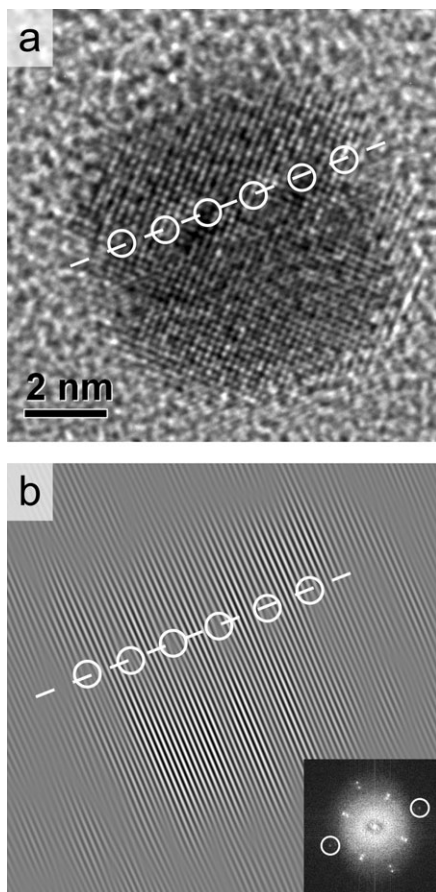


Fig. 3 (a) High resolution image of a CuAg nanoparticle with Ag located on the upper side and Cu on the lower side of the particle. The (220) interface plane is represented by a dotted line. The misfit dislocations are localized by white circles along the interface plane. (b) Bragg-filtered image using the 220 reflection that allows the excess Cu planes of the perfect misfit dislocations to be seen. The inset represents the power spectrum of micrograph (a) on which the two 220 reflections used for the filtering are circled.

critical thickness t_c is roughly given by:

$$t_c = b/\varepsilon$$

where b is the Burger's vector modulus ($1/2 [110]$ for the FCC structures) and ε the misfit between the two lattice parameters defined by $\varepsilon = (a_{\text{Ag}} - a_{\text{Cu}})/a_{\text{Cu}}$. Applying this model leads to a critical thickness close to 2 nm, to be compared with the thickness of the Ag layer on Fig. 3a which is around 2.5 nm.

2. Cu morphological transitions

From Fig. 1d, it is worth noting that the core/shell nanoparticle sizes are the smallest (< 12 nm) from the size distribution of the nanoparticles. Over this limit, most of the CuAg nanoparticles do not present the core/shell configuration. The size of the pre-existing Cu cores being unambiguously an important parameter in the formation of the core/shell arrangement, we turned to the structural characterisation of the Cu cores alone, especially under the identified size limit. Controlling the size of the Cu nanoparticles can be achieved by two different means. The first would be to lower the

substrate temperature during the formation of the Cu core, decreasing the Cu diffusion on the surface. Cu atoms would then be fixed more efficiently on the nucleating sites, resulting in an increased number of particles per unit area, and subsequently smaller particle sizes. The second is to decrease the quantity of matter during deposition, keeping constant all the other parameters, especially the substrate temperature. The density of particles per square nanometer remains the same, and the mean nanoparticle size decreases because of the lack of atoms available for the growth. As for gold, Cu exhibits some morphological transitions between three different types: (1) an icosahedral shape constituted by 20 slightly distorted FCC tetrahedra gathered to form a 20 faces polyhedron; (2) a decahedral shape formed by 5 identical FCC sectors separated by imperfect twins, giving a 5-fold symmetry polyhedron; and (3) a rounded or faceted monocrystalline FCC structure. These transitions have been predicted using tight-binding semiempirical potentials for metal–metal interactions²³ and observed in a number of published papers, for clusters either free or supported on a substrate. We conducted HRTEM experiments on a sample with 2 nm of Cu deposited at 400 °C to check whether the synthesis method used here reproduces the same morphological transitions. The work by Koga *et al.*²⁴ was very helpful in identifying the different morphologies by interpreting the lattice fringe contrast on the HRTEM images. Although a good statistical sampling is difficult to realize, we obtained the following results, collected in Fig. 4.

Due to the relatively broad size distribution of the Cu nanoparticles, it is clear that the three types of morphologies and structures are present on the substrate, with a strong overlapping between icosahedral and decahedral domains. The transition from decahedra to monocrystalline FCC structures is sharper, with FCC Cu nanoparticles sizes starting from 8 nm. The size limit over which core/shell

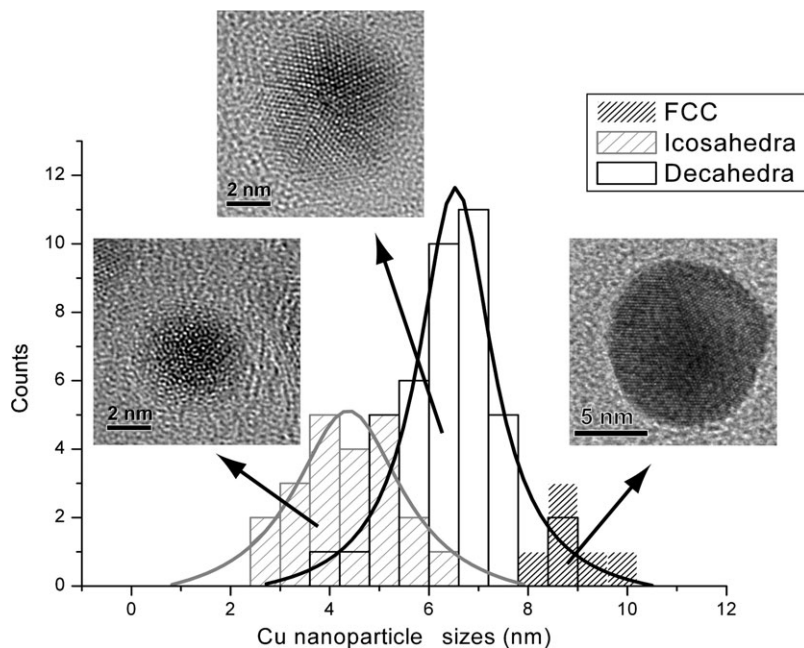


Fig. 4 Size distributions of the three different morphologies identified on a sample with 2 nm of Cu deposited at 400 °C. These distributions were obtained from conventional and high resolution TEM images. For each size range, a typical HRTEM image of a nanoparticle is shown.

arrangements are no more formed corresponds well to the decahedra-to-FCC structural transition.

3. Dependence with Cu core sizes

We carried out two other experiments to confirm that a Cu core size under 12 nm is the key parameter to obtain core/shell nanoparticles. The parameters were adjusted to obtain on one hand a Cu core size distribution centred under 12 nm, and on the other hand a distribution largely over 12 nm.

The first CuAg system has been synthesized with nominal thickness of 2 nm and 1 nm for, respectively Cu and Ag (denoted 2@1 in the following), keeping a substrate temperature of 400 °C and a constant ratio between the Cu and Ag nominal thicknesses. An EFTEM image corresponding to this system is presented on Fig. 5a. A majority of the nanoparticles present a core/shell configuration, with core sizes below 12 nm and shell thickness distribution centred on 2 nm (values ranging between 1 nm and 3.5 nm). The thickness of the Ag shell was determined by the width of the intensity profile on the EFTEM Ag chemical maps. On the same area of the microscopy grid corresponding to the 2@1 system, size counting on the EFTEM

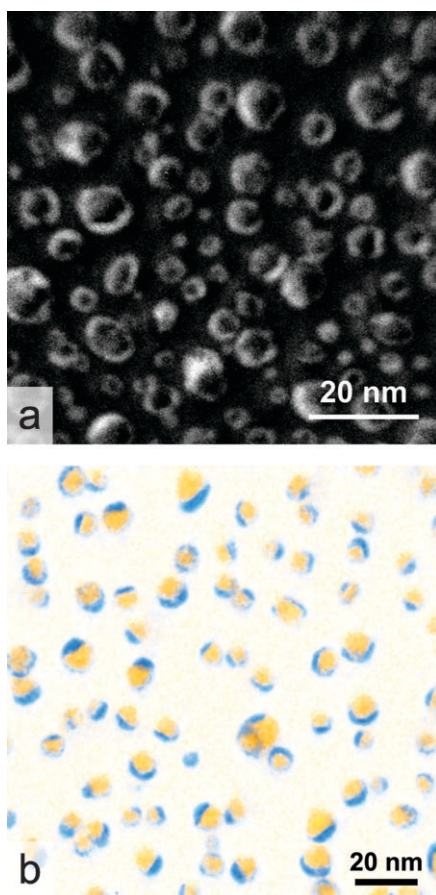


Fig. 5 (a) Ag chemical map obtained by EFTEM, corresponding to the 2@1 system deposited with a substrate temperature of 400 °C. (b) Colour-coded chemical map with Ag (blue) and Cu (yellow) obtained by EFTEM, corresponding to the 2@1 system deposited with a substrate temperature of 500 °C.

and TEM images as well as statistical measurements using a micro-Raman probe¹³ have been carried out. The statistical approach confirms the local measurements.

The second experiment aimed at the formation on the substrate of Cu cores with sizes over 12 nm. This was achieved by depositing the same Cu thickness (2 nm), but with a substrate temperature of 500 °C (Fig. 5b). For Ag, no difference was noticed in the final microstructure between a deposition at a substrate temperature of 500 °C (as for Cu) and a deposition after cooling down to 400 °C. Almost no particles present a core/shell structure, which confirms the assumption of a Cu core size limit for the core/shell formation. The explanation must be linked to the way silver grows on the Cu nanoparticles. From crystal growth theory, it is well known that the growth rate is different depending on the Miller indices of the face exposed to incoming species. This remark must be related to the fact that for an icosahedron, all the faces present the same crystallographic orientation, that is (111) faces. For a decahedron, the two bases are also (111) faces, and depending on the growth along the 5-fold axis, the decahedron show (100) lateral faces. The situation is completely different for the monocrystalline FCC structure: the nanoparticles exhibit either no faceting, or faces typical from a cuboctahedron which show (111), (200) and (220) faces. For the two morphologies corresponding to sizes less than 10 nm, the growth of the Ag shell will be far more isotropic, and hence the thickness will be more homogeneous all around the Cu cores. This hypothesis is sustained by HRTEM observations on the 2@1 system deposited with a substrate temperature of 400 °C. Fig. 6 shows an example of a Cu decahedron with a complete Ag shell all over the particle. The Moiré patterns evidence the presence of Ag in an epitaxial relationship with the five subjacent Cu sectors. The [110] zone axis for the five different FCC sectors composing the decahedron are visible on the power spectrum presented on Fig. 6b.

Moreover, Moiré patterns stop before the edges of the particles, which means that only Ag is present on the edges, hence forming a continuous shell all around the particle. The shell thickness on this image (Fig. 6a) can then be estimated to about 2 nm. This is the limit predicted by the critical thickness model (Section C.1) over which the Ag shell is relaxed to its bulk lattice parameter.

D. CoPt bimetallic alloyed nanoparticles

This part focuses on the influence of the nature of the substrate (a-Al₂O₃ or a-carbon) and the synthesis parameters on the growth and the structure of CoPt nanoparticles. Bulk equiatomic CoPt exhibits a phase transition at 825 °C, between a tetragonal ordered phase (L1₀) at low temperature and a disordered FCC structure at high temperature.²⁵ The L1₀ ordered phase, due to the alternative atomic stacking of pure Co and pure Pt layers, has large magnetocrystalline anisotropy. By means of this property, important research efforts are devoted to study L1₀ ordered CoPt nanoparticles which are expected to be the future information storage media for extremely high density recording (EHDR).^{26,27} The diffraction pattern of this structure presents superstructure reflections characterizing the ordered structure.

1. Influence of the substrate on nanoparticle growth

CoPt nanoparticle thin films with 2 nm nominal thickness have been prepared at a substrate temperature of 550 °C with a laser frequency of 5 Hz on a-carbon and a-Al₂O₃ substrates. Fig. 7a and b show TEM bright field images of the CoPt nanoparticles prepared on the a-carbon and the a-Al₂O₃ substrates, respectively. The mean size, the polydispersity (standard deviation divided by the mean size of the nanoparticles), the particle density and the coverage ratio for each sample are given in Table 1.

The coverage ratio, defined as the percentage of the covered surface of the substrate by the nanoparticles, has been determined from TEM bright field images

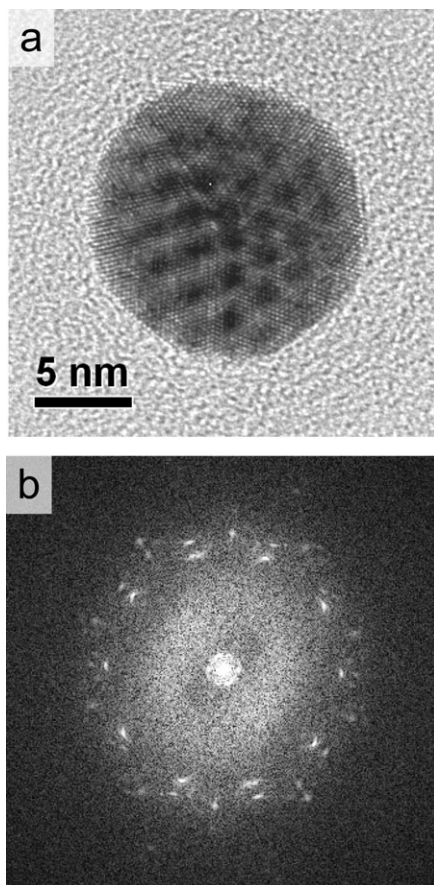


Fig. 6 (a) High resolution micrograph of a CuAg core/shell decahedron with Moiré patterns on each of the five FCC sectors. (b) Power spectrum of micrograph (a).

using Digital Micrograph software. Note that the contrast of particles smaller than 2 nm is too weak to consider them in the statistical characterisation.

The growth mechanisms involved in a PLD experiment are quite different from those observed in classical thermal evaporation techniques because the flux of atoms is discontinuous. These mechanisms can be described as follow: firstly, nucleation and size increase of the *nuclei* under high flux of atoms during the deposition time (*i.e.* several μs) and secondly, coalescence and Ostwald ripening between two pulses (*i.e.* several 0.1 s). The coalescence takes place by atomic rearrangement of two close enough nanoparticles, leading to the formation of atoms inter-diffusion bridges.²⁸ The Ostwald ripening implies the growth of large particles at the expense of the ones smaller than the critical nuclei.²⁹ In the case of PLD, due to the rapid decrease of supersaturation after a laser pulse, these two mechanisms occur alone over a long time and influence the nanoparticle morphology. As a consequence, in the late stage of the synthesis, new nucleation sites become available on the substrate between the biggest particles, making possible the growth of smaller CoPt nanoparticles. This explains the high polydispersity observed on the a-carbon substrate that shows a high number of very small particles in the range size from 2 nm to 4 nm (inset Fig. 7a). This phenomenon is less important in the case of the a- Al_2O_3 substrate (inset Fig. 7b). It suggests that the diffusion of Co and Pt on a-carbon substrate is higher than the ones on a- Al_2O_3 .

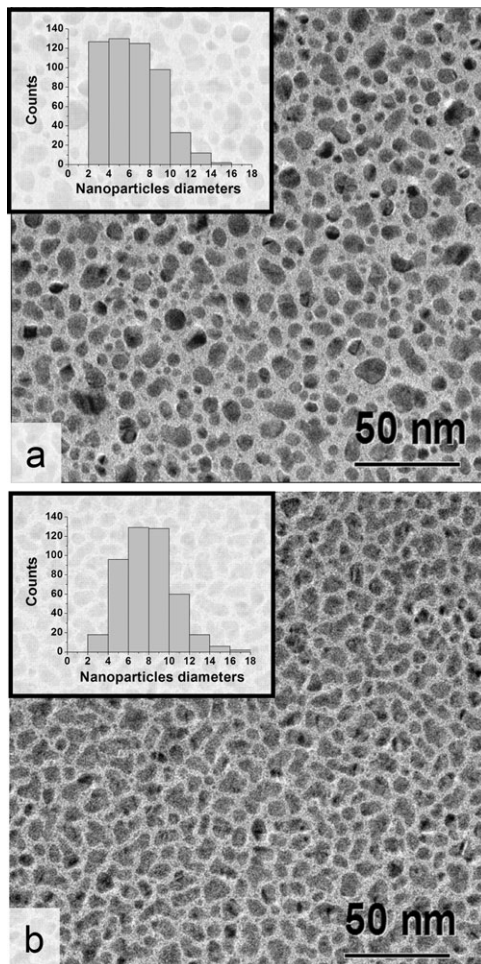


Fig. 7 CoPt FCC disordered nanoparticles synthesized by PLD at 550 °C with in the insets the size distribution of the particles. (a) Substrate: 10 nm thick amorphous carbon film on a commercial TEM grid. (b) Substrate: 2 nm thick amorphous alumina film deposited by PLD on the carbon film of a commercial TEM grid.

Since the nominal thickness is the same for both samples, by comparing the mean size and the coverage ratio of CoPt nanoparticles on a-carbon and on a-Al₂O₃, we can deduce that the nanoparticles are more flattened on a-Al₂O₃ substrate than on a-carbon substrate. This difference is closely related to the kinetic barriers involved during the nanoparticle formation. Kinetic energy of the atoms, given by the substrate temperature governs the ability to overcome the various diffusion barriers (metal–metal and metal–substrate upstepping and downstepping activation

Table 1 Mean size, polydispersity, particle density and coverage ratio of the samples prepared at 550 °C, with a laser frequency of 5 Hz on a-carbon and a-Al₂O₃ substrates

2 nm of CoPt on substrate	Mean size/nm	Polydispersity (%)	Particles density (10 ² part. μm ⁻²)	Coverage ratio (%)
a-Carbon	6.3	45	110	42
a-Al ₂ O ₃	7.9	30	90	50

energies).^{30,31} At a given temperature, these diffusion barriers control the evolution of film morphology during the growth. From our experimental results, the two-dimensional growth on alumina may then be the signature either of strong interactions of CoPt with alumina (higher activation barrier for the 3-dimensional growth compared to carbon) or a lower effective substrate temperature in the case of alumina. To summarize, we show here that the kind of interactions between the substrate and the species deposited drive both the size distribution and the morphologies of the nanoparticles: the 3-dimensional growth of the nanoparticles is promoted on a-carbon whereas a-Al₂O₃ substrate minimizes the size dispersion. The following question remains: how can we know if the diffusion and the substrate–metal upstepping energy of the Co and Pt atoms are retained by a stronger a-Al₂O₃–metals interaction, or slowed down by the lower temperature of the alumina surface?

It is thus important to emphasise the thermal properties of the substrate, which are generally not taken into account enough in nanoparticle synthesis on either monocrystalline or amorphous substrates. Contrary to carbon, alumina is a good thermal insulator. As a rough indication, the heat capacity, at room temperature, of the crystalline alumina (79.45 J mol⁻¹ K⁻¹) is almost ten times higher than the one of graphite (8.58 J mol⁻¹ K⁻¹).³² This property of alumina is well known since in the electronic and optic industries, amorphous alumina thin films are promising materials for thin thermal insulator layers.³³ However, it is difficult to differentiate the respective role of the strong interactions of the deposited species with the substrate and low thermal conductivity of the a-Al₂O₃ layer, because they both have the same influence on the morphology of CoPt nanoparticles.

2. Thermal insulator properties of a-Al₂O₃ substrate

To demonstrate the strong influence of the thermal conductivity of the substrate, we have synthesized nanoparticles on a-Al₂O₃ with the same experimental conditions than the ones used for the synthesis of nanoparticles shown in Fig. 7b. However, we have increased the thickness of the a-Al₂O₃ substrate to 10 nm. As can be seen in Fig. 8, the particles are very close to the percolation threshold with irregular shapes elongated in the plane of the substrate. These flat morphologies compared to Fig. 7b indicate the tendency of the metals to wet the surface because the thermal energy brought to the system is not high enough to permit 3D growth mechanism. The coverage ratio of 80% is close to the one obtained on particles formed on a 2 nm thick a-Al₂O₃ layer heated at 400 °C. The particle morphologies studied as a

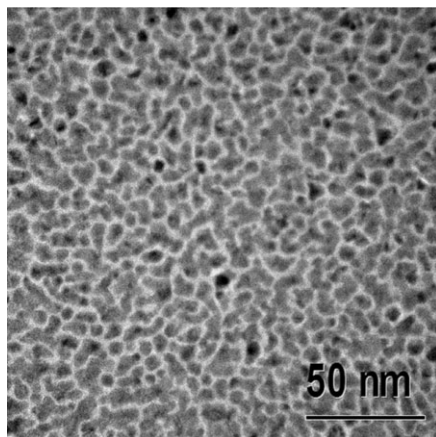


Fig. 8 CoPt nanoparticles, with a 2 nm nominal thickness, synthesized by PLD on a 10 nm thick amorphous alumina layer deposited by PLD on the carbon film of a commercial TEM grid heated at 550 °C.

function of the a-Al₂O₃ layer thickness clearly show the thermal influence of this substrate.

3. Thermal influence of the substrate on the structure of the nanoparticles

The structure of previous samples ($T_s = 550\text{ }^\circ\text{C}$) was FCC disordered which is a non equilibrium phase compared to the bulk material phase diagram. This FCC structure appears using the PLD synthesis route because the growth kinetics of the particles is faster than the ordering kinetics. To obtain as-grown L1₀ ordered nanoparticles, the substrate has to be heated over 650 °C.¹⁸ At $T_s = 550\text{ }^\circ\text{C}$, the ordering mechanisms require a post-synthesis annealing. CoPt nanoparticles, prepared in the same conditions as the ones studied in part D1, were annealed over 2 h at 550 °C and were then covered by a thin a-Al₂O₃ layer after the annealing. Fig. 9a and b show the morphology of the nanoparticles after the annealing on the a-carbon and a-Al₂O₃ substrates, respectively. Since substrates are amorphous, the nanoparticles are randomly oriented on the surface and the diffraction patterns display a typical ring pattern characteristic of a powder-like diffraction. Because of the very weak intensity of the superstructure reflections (see inset of Fig. 9c), we used imaging plate detectors which have a very high sensitivity and a large dynamic range. Moreover, to highlight the recorded intensity we performed a rotational averaging intensity profile using Process Diffraction software. This intensity profile is drawn as a function of the modulus of the diffraction vector $g = 2\pi/d$ where d is the interplanar distance. Fig. 9c and d show, respectively averaging plots corresponding to the diffraction patterns

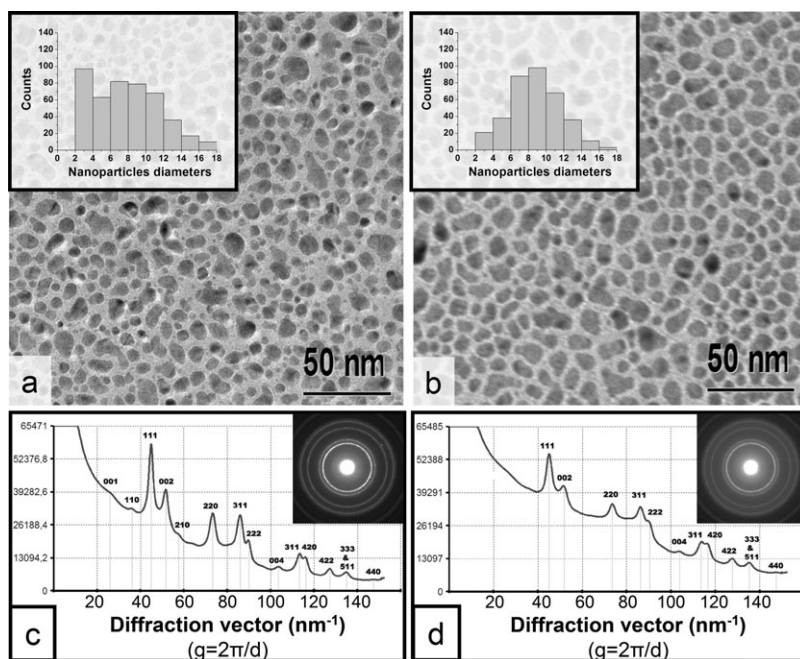


Fig. 9 CoPt nanoparticles deposited by PLD with a laser frequency of 5 Hz (30 min) on a substrate heated at 550 °C and then annealed in the deposition chamber at 550 °C during 2 h. In the inset: size distribution of the particles. (a) Substrate: 10 nm thick amorphous carbon film of a commercial TEM grid. (b) Substrate: 2 nm thick amorphous alumina film of deposited by PLD on the carbon film of a commercial TEM grid. Electron diffraction patterns of CoPt nanoparticles grown (30 min) and annealed (120 min) at 550 °C, and their corresponding rotational averaging profiles. (c) Ordered L1₀ nanoparticles on amorphous carbon film. (d) Disordered FCC nanoparticles on amorphous alumina film.

of each sample: CoPt/a-carbon and CoPt/a-Al₂O₃. All rings are indexed according to the FCC disordered or the L1₀ ordered structures of the CoPt system.

The diffraction pattern of the particles annealed over 2 h after their synthesis on a-carbon presents the 001, 110 and 211 superstructure reflections characteristic of the L1₀ ordered lattice. On the contrary, the diffraction pattern of particles grown and annealed on a-Al₂O₃ presents only the fundamental reflections of the FCC disordered structure. This result has been confirmed by HRTEM. Energy Dispersive X-ray (EDX) analyses show that particles are close to the equiatomic composition on both samples. The annealed particles mean size is smaller on a-carbon (7.8 nm) than the one on a-Al₂O₃ (8.8 nm). We can then rule out the possibilities that the different structural states observed on both samples are due to deviation of the composition of the CoPt particles or to size effects. During the annealing, the contact surface between the substrate and the particles is limited. Taking into account the particle size, the proportion of atom linked to the substrate is too low to consider a strong influence of the chemical interaction on the ordering of the particles. It still requires an assumption to explain this difference: the thermal insulator properties of amorphous alumina.

During the annealing, the increase of the mean particle size on a-carbon (20%) is twice as high as the one of the particles on a-alumina (10%). It shows the low diffusion of Co and Pt atoms on a-Al₂O₃ substrate. These alumina properties have been highlighted already by Takahashi *et al.*³⁴ who compared the morphology of FePt nanoparticles after an annealing of 1 h at 600 °C in MgF₂ and a-Al₂O₃ matrix. They showed that the covering alumina layer reduces the coalescence and Oswald ripening phenomena avoiding the size increase of particles. Then they explained by size effects the disordered structure of the particles in alumina compared with the ordered ones in MgF₂ but they did not consider the eventually different effective particle temperature. The goal of our structural studies is not to deny their interpretation but to emphasize the strong influence of the thermal properties of the substrate.

4. Influence of the laser frequency on the growth and the structure of the nanoparticles

The influence of the laser frequency in the PLD experiment can be seen by comparing the morphology and structure obtained with a laser frequency of 5 Hz (Fig. 7a) with the ones obtained with a lower frequency. We have synthesized a sample of 2 nm nominal thickness prepared on a-carbon substrate heated at 550 °C with a laser frequency of 1 Hz. Fig. 10a shows a TEM bright field image of this nanoparticle thin film. By decreasing the laser frequency from 5 to 1 Hz, we have increased the polydispersity from 45 to 66% and the mean size from 6.3 to 9.2 nm. With a 1 Hz laser frequency, the time between two pulses is five times longer than the time at 5 Hz. As a consequence, the histogram in the inset of Fig. 10a shows clearly a bimodal size distribution, the first population has a mean size of 3 nm whereas the second one has a mean size of 13 nm. It is the signature of the Oswald ripening and coalescence mechanisms which occur over a longer time which influence the particle morphology. The synthesis of samples takes 30 min and 150 min, using a laser frequency of 5 Hz and 1 Hz, respectively. To dissociate the laser frequency effect from the synthesis time effect, we compared nanoparticles synthesized with a laser frequency of 5 Hz and annealed at 550 °C during 120 min (Fig. 9a), to ones obtained with a laser frequency of 1 Hz (Fig. 10a). The higher mean size and polydispersity of the latter clearly show the influence of the laser frequency. The Oswald ripening and coalescence phenomena during the deposition at 1 Hz (150 min) are more effective than those occurring during the synthesis at 5 Hz (30 min) and the post synthesis annealing (120 min).

The shape of the nanoparticles, fabricated with a 1 Hz laser frequency, has been determined by means of a 3D electron tomography experiment. The electron

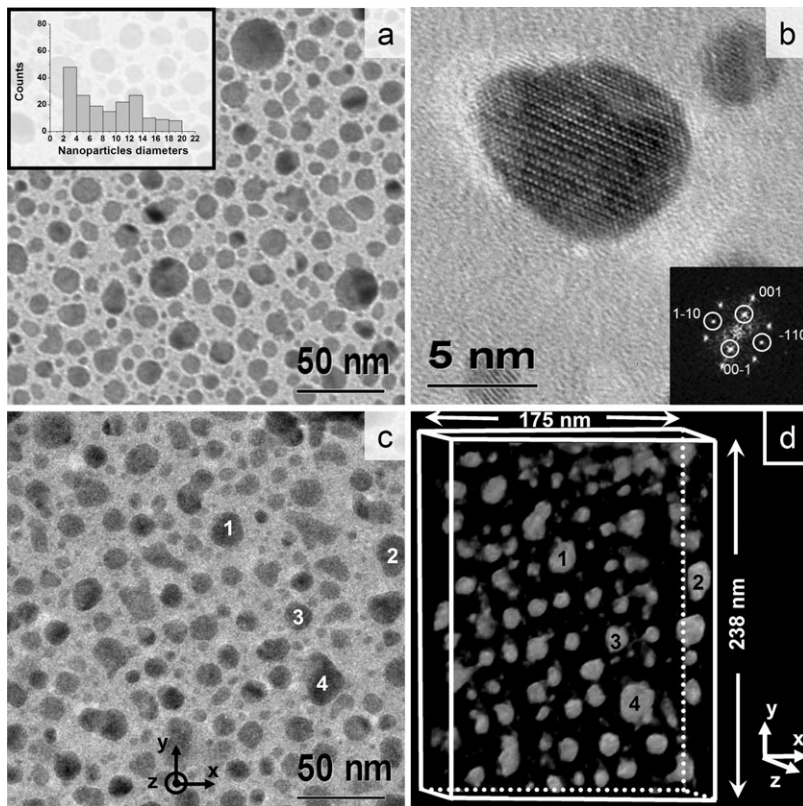


Fig. 10 Ordered $L1_0$ CoPt nanoparticles synthesized by PLD with a laser frequency of 1 Hz (2h30) on amorphous carbon film at a temperature of 550 °C. (a) BF image of the nanoparticles. (b) HRTEM image of a CoPt $L1_0$ ordered nanoparticle oriented along the [110] direction, with in the inset the power spectrum on the image where the superstructure reflections are encircled. (c) TEM images of the selected area for the tomography experiment, (d) 3D reconstruction of the selected area obtained by electron tomography. The correspondence between 2D images of the particles and the 3D volumes is emphasized by the numbers on these two images.

tomography technique allows the 3D morphology to be reconstructed from 2D observations of the nanoparticles. One or several series of projections of the nanoparticles have to be recorded in bright field imaging conditions. Such a series of projections is obtained by tilting the specimen in a range from -70° to 70° with respect to the electron beam and taking an image for each tilt angle. Once the series of projections is recorded, the reconstruction of the object is computed by using a back-projection algorithm.³⁵ A bright field image of the selected area is presented in Fig. 10c and its 3D representation (tomogram) is presented in Fig. 10d. The thickness of the particles has been measured by slicing the tomogram in the two perpendicular x and y directions (Fig. 10d). The thickness of the nanoparticles are measured directly on the sliced images, corresponding to the (x,z) or the (y,z) planes, by the size of the nanoparticles along the z direction. For 80% of the nanoparticles, the measured thickness is equal to the diameter in the plane of the substrate. It can be explained by the 3D growth mechanisms involved between two pulses (metal-metal and metal-substrate upstepping), discussed in part D1. The shape of the last 20% of the nanoparticles, which is larger than thick, results from coalescence mechanisms.

A low laser pulse frequency during the growth also influences the structure of the nanoparticles. With a laser frequency of 1 Hz and $T_s = 550\text{ }^\circ\text{C}$, the $L1_0$ structure is stabilized without further annealing. This result has been observed from electron diffraction of the particles and Fig. 10b shows a HRTEM image of a single $L1_0$ ordered CoPt nanoparticle oriented along the $[110]$ zone axis. In such images, the order is clearly evidenced by the succession of bright and dark fringes which can be related to the stacking of pure Co and Pt planes along the $[001]$ direction as indicated by the power spectrum of the image given in the inset of Fig. 10b.

To conclude, when decreasing the laser frequency, we reduce the nanoparticle growth kinetics, which is then slower than the ordering one. In these conditions, the diffusion of the metallic atoms at $550\text{ }^\circ\text{C}$ allows us to obtain as-grown nanoparticles with the $L1_0$ equilibrium structure according to the bulk phase diagram.

Conclusion

Growth and structural properties of immiscible CuAg and alloyed CoPt nanoparticles have been studied. In CuAg, prepared by TE, the Ag layer is completely relaxed when its thickness is equal to 2 nm. The mechanism involved in the stress relaxation has been demonstrated to be the same as the one occurring in thin film epitaxy. We have shown that there is a critical size for the Cu core, up to which the formation of the core/shell arrangement is promoted. This configuration is probably favoured by the underlying morphologies of the Cu cores which present icosahedral and decahedral configurations under a size smaller than 8 nm. Such shapes are mainly constituted of (111) faces implying that the growth rate of the Ag layer is the same on all these faces.

In CoPt, prepared by PLD, the morphology and the structure of the nanoparticles has been investigated as a function of the nature of the substrate and the laser frequency. The diffusion of Co and Pt atoms is favoured on α -carbon compared to amorphous alumina, or by using a lower frequency during the deposition process. These phenomena result from the competition between the kinetic energy of the atoms, given by the substrate temperature, and the kinetic barriers, depending on the metal/substrate interaction, which drive the formation of 3D morphologies. The thermal properties of the substrate can have a strong influence on the structure of the nanoparticles. Finally, we have shown that it is possible to synthesize as-grown ordered $L1_0$ CoPt nanoparticles by reducing the growth kinetics (*i.e.* by decreasing the laser frequency).

References

- 1 S. Sao-Joao, S. Giorgio, J. M. Penisson, C. Chapon, S. Bourgeois and C. Henry, *J. Phys. Chem. B*, 2005, **109**, 342.
- 2 B. Skarman, T. Nakayama, D. Grandjean, R. E. Benfield, E. Olsson, K. Niihara and L. R. Wallenberg, *Chem. Mater.*, 2002, **14**, 3686.
- 3 N. Toshima, *Pure Appl. Chem.*, 2000, **72**, 317.
- 4 N. Toshima, M. Harada, Y. Yamazaki and K. Asakura, *J. Phys. Chem.*, 1992, **96**, 9927.
- 5 L. Favre, S. Stanesco, V. Dupuis, E. Bernstein, T. Epicier, P. Melinon and A. Perez, *Appl. Surf. Sci.*, 2004, **226**, 265.
- 6 H. Zeng, J. Li, Z. L. Wang, J. P. Liu and S. Sun, *Nano Lett.*, 2004, **4**, 187.
- 7 S. Basu and D. Chakravorty, *J. Non-Cryst. Solids*, 2006, **352**, 380.
- 8 M. Gaudry, E. Cottancin, M. Pellarin, J. Lerme, L. Arnaud, J. R. Huntzinger, J. L. Vialle, M. Broyer, J. L. Rousset, M. Treilleux and P. Melinon, *Phys. Rev. B: Condens. Matter Mater. Phys.*, 2003, **67**, 155409.
- 9 J. Zhu, Y. Wang, L. Huang and Y. Lu, *Phys. Lett. A*, 2004, **323**, 455.
- 10 D. Garcia-Gutierrez, C. Gutierrez-Wing, M. Miki-Yoshida and M. Jose-Yacamán, *Appl. Phys. A: Mater. Sci. Process.*, 2004, **79**, 481.
- 11 S. Sun, C. B. Murray, D. Weller, L. Folks and A. Moser, *Science*, 2000, **287**, 1989.
- 12 S. P. Withrow, C. W. White, J. D. Budai, L. A. Boatner, K. D. Sorge, J. R. Thompson and R. Kalyanaraman, *J. Magn. Magn. Mater.*, 2003, **260**, 319.

-
- 13 M. Cazayous, C. Langlois, T. Oikawa, C. Ricolleau and A. Sacuto, *Phys. Rev. B*, 2006, **73**, 113402.
 - 14 T. Miyazaki, O. Kitakami, S. Okamoto, Y. Shimada, Z. Akase, Y. Murakami, D. Shindo, Y. K. Takahashi and K. Hono, *Phys. Rev. B*, 2005, **72**, 144419.
 - 15 K. Sato, B. Bian, T. Hanada and Y. Hirotsu, *Scripta Materialia*, 2001, **44**, 1389.
 - 16 L. Castaldi, K. Giannakopoulos, A. Travlos and D. Niarchos, *Appl. Phys. Lett.*, 2004, **85**, 2854.
 - 17 D. B. Chrisey and G. K. Hubler, *Pulsed Laser Deposition of Thin Films*, John Wiley & Sons, London, 1994.
 - 18 D. Alloyeau, C. Langlois, C. Ricolleau, Y. Le Bouar and A. Loiseau, *Nanotechnology*, 2007, **18**(37), 375301.
 - 19 T. W. Trelenberg, L. N. Dinh, B. C. Stuart and M. Balooch, *Appl. Surf. Sci.*, 2004, **229**, 268.
 - 20 L. Vitos, A. V. Ruban, H. L. Skriver and J. Kollar, *Surf. Sci.*, 1998, **411**, 186.
 - 21 J. P. Hirth and J. Lothe, *Theory of Dislocations*, Krieger Publishing Company, Berlin 1982.
 - 22 A. E. Romanov, W. Pompe, S. Mathis, G. E. Beltz and J. S. Speck, *J. Appl. Phys.*, 1999, **85**, 182.
 - 23 C. Mottet, J. Goniakowski, F. Baletto, R. Ferrando and G. Treglia, *Phase Transitions: Multimatl. J.*, 2004, **77**, 101.
 - 24 K. Koga and K. Sugawara, *Surf. Sci.*, 2003, **529**.
 - 25 Y. Le Bouar, A. Loiseau and A. Finel, *Phys. Rev. B*, 2003, **68**, 224203.
 - 26 D. J. Sellmyer, M. Yu and R. D. Kirby, *Nanostruct. Mater.*, 1999, **12**, 1021.
 - 27 M. Yu, Y. Liu and D. J. Sellmyer, *J. Appl. Phys.*, 2000, **87**, 6959.
 - 28 G. Palasantzas, T. Vystavel, S. A. Koch and L. T. D. Hosson, *J. Appl. Phys.*, 2006, **99**, 024307.
 - 29 I. M. Lifshitz and V. V. Slyozov, *Sov. Phys. JETP*, 1959, **35**, 331.
 - 30 C. T. Campbell, *Surf. Sci. Rep.*, 1997, **27**, 1.
 - 31 C. R. Henry, *Surf. Sci. Rep.*, 1998, **31**, 231.
 - 32 D. R. Lide, *CRC Handbook of Chemistry and Physics*, CRC press, London, 2002–2003.
 - 33 B. Behkam, Y. Yang and M. Asheghi, *Int. J. Heat Mass Transfer*, 2005, **48**, 2023.
 - 34 Y. H. Takahashi, T. Ohkubo, M. Ohnuma and K. Hono, *J. Appl. Phys.*, 2003, **93**, 7166.
 - 35 B. F. Mc Ewen and M. Marko, *J. Histochem. Cytochem.*, 2001, **49**, 553.